Heterophilic cell–cell adhesion of atypical cadherins Fat and Dachsous regulate epithelial cell size dynamics during *Drosophila* thorax morphogenesis

Amit Kumar[†,‡], Mohd Suhail Rizvi[†,§], Thamarailingam Athilingam[†,||], Saurabh Singh Parihar, and Pradip Sinha*
Department of Biological Sciences and Bioengineering, Indian Institute of Technology, Kanpur, Uttar Pradesh 208016, India

ABSTRACT Spatiotemporal changes in epithelial cell sizes—or epithelial cell size dynamics (ECD)—during morphogenesis entail interplay between two opposing forces: cell contraction via actomyosin cytoskeleton and cell expansion via cell–cell adhesion. Cell–cell adhesion–based ECD, however, has not yet been clearly demonstrated. For instance, changing levels of homophilic E-cadherin-based cell–cell adhesion induce cell sorting, but not ECD. Here we show that cell-expansive forces of heterophilic cell–cell adhesion regulate ECD: higher cell–cell adhesion results in cell size enlargement. Thus, ECD during morphogenesis in the heminotal epithelia of *Drosophila* pupae leading to thorax closure corresponds with spatio-temporal gradients of two heterophilic atypical cadherins—Fat (Ft) and Dachsous (Ds)—and the levels of Ft–Ds heterodimers formed concomitantly. Our mathematical modeling and genetic tests validate this mechanism of dynamic heterophilic cell–cell adhesion–based regulation of ECD. Conservation of these atypical cadherins suggests a wider prevalence of heterophilic cell–cell adhesion–based ECD regulation during animal morphogenesis.

INTRODUCTION

In an epithelium, subapical adherens junctions (AJs) represent focal zones of both cadherin-mediated cell–cell adhesion and actomyosin network-linked intracellular contractility. These opposing forces of cell contractility and cell–cell adhesions at AJs have long been proposed to regulate cell size and shape (for recent reviews, see

Lecuit and Lenne, 2007; Heisenberg and Bellaïche, 2013; Pinheiro and Bellaïche, 2018). Spatiotemporal modulations of epithelial cell sizes—which we term here as epithelial cell size dynamics (ECD)—are a common observation during epithelial morphogenesis (Pinheiro and Bellaïche, 2018). Regulation of cell contractility at AJs finds a ready connection to ECD during tissue morphogenesis. For instance, cell contraction mediated by nonmuscle myosin II (Myo-II) reduces apical cell sizes by apical constriction, leading to tissue folding during *Drosophila* gastrulation (Martin *et al.*, 2009). Further, recent computational modeling has revealed aspects of tissue dynamics that are regulated by cell contractility. For instance, simulation of protein trafficking between apical and medial cell membrane domains and their cross-talk with actomyosin networks reveal mechanistic underpinnings of oscillations in cell area seen during dorsal closure (Durney *et al.*, 2018). Further, modeling of two-way feedback between Rho GTPases signaling and mechanical tension—in the context of spatially varying levels of cell–cell adhesions—could recapitulate the tissue dynamics seen in collective cell migrations during epithelial morphogenesis (Zmurchok *et al.*, 2018).

In contrast, the contribution of cell–cell adhesion to tissue dynamics has not been sufficiently examined yet. Prevailing observations on differential cell–cell adhesion—such as that mediated

by cadherins—explain cell sorting (Foty and Steinberg, 2005) as seen in a diverse range of morphogenetic processes during animal development (reviewed in Keller, 2002; Gumbiner, 2005; Halbleib and Nelson, 2006). In *Drosophila*, examples of differential adhesion-mediated cell sorting are seen during oogenesis when up-regulation of DE-cadherin in the oocyte facilitates its sorting from the germline cells (Godt and Tepass, 1998). Likewise, during retinal development, selective expression of N-cadherins in the cone cells leads to their sorting from other pigment cells, which uniformly express DE-cadherin (Hayashi and Carthew, 2004). Further, subtle changes in cell–cell adhesion could also contribute to cell neighbor exchanges during cell intercalations and during the germ band extension stage in the *Drosophila* embryo (Lecuit, 2005). These examples of differential cell adhesion, however (Foty and Steinberg, 2005; Halbleib and Nelson, 2006; Lecuit and Lenne, 2007), do not reveal how cell–cell adhesion could be dynamically regulated leading to ECD—sans cell sorting—during epithelial morphogenesis.

Because ECD by definition is spatiotemporal in nature, a prerequisite for its candidate regulators will necessarily be their dynamic pattern of expression, both spatially and temporally. The well-known homophilic regulator of epithelial cell–cell adhesion, DE-cadherin, however (see Keller, 2002; Gumbiner, 2005; Halbleib and Nelson, 2006), does not display spatial modulations during development of adult epithelial primordia in *Drosophila*: for instance, in the pupal heminotal epithelium (Supplemental Figure S1, A and B). Previously, a correlation between tapering gradients of the Wg ligand and DE-cadherin with cell sizes was seen in the developing wing imaginal disc epithelium (Jaiswal *et al.*, 2006; Somorjai and Martinez-Arias, 2008; Widmann and Dahmann, 2009). Similar observations in *Drosophila* cell lines were also reported (Wodarz *et al.*, 2006). However, these observations do not quite translate into spatiotemporal regulation of DE-cadherin commensurate with ECD in the developing epithelial primordia in *Drosophila*. In contrast, an atypical cadherin, Dachsous (Ds)—which binds in a heterophilic manner with another atypical cadherin, Fat (Ft)—displays spatial regulation in imaginal disc epithelia (Clark *et al.*, 1995; Ma *et al.*, 2003). Both Ft and Ds display large numbers of extracellular cadherin repeats, which form adhesive Ft–Ds heterodimers in a subapical domain above the AJs with neighboring cells (Ma *et al.*, 2003). Cellular and morphogenetic fallout of formation of Ft–Ds heterodimers has many forms. For instance, asymmetric enrichment of Ft–Ds heterodimers at the proximal and distal edges of epithelial cells in an epithelium provides cues to their collective orientation, orthogonal to the apicobasal axis, which is termed planar cell polarity (PCP; for recent reviews, see Goodrich and Strutt, 2011; Matis and Axelrod, 2013; Devenport, 2014; Butler and Wallingford, 2017).

In the context of the present study, however, the most interesting fallout of Ft–Ds heterodimer formation—as originally predicted (Clark *et al.*, 1995)—is cell–cell adhesion. For instance, *Drosophila* S2 cell lines upon cotransfection with Ft and Ds display cell–cell adhesion (Matakatsu and Blair, 2004, 2006). Likewise, in mammalian cell lines, cotransfection with Fat4 and Dchs1 leads to formation of Fat4–Dchs1 stable complexes at the cell boundary, thereby displaying cell–cell adhesion (Loza *et al.*, 2017). Further, somatic clones displaying loss of Ft in the wing imaginal disc epithelium sort out from their neighbors as a result of altered cell–cell adhesion, besides displaying reduction in their cell sizes (Jaiswal *et al.*, 2006). Given the spatial regulation of Ds and Ft–Ds heterodimer-mediated cell–cell adhesion, in a hypothesis-driven approach, here we have examined whether Ft and Ds atypical cadherins represent the elusive regulators of ECD during morphogenesis of the adult thorax in *Drosophila* pupa.

Here we show that morphogenesis of heminotal epithelia during thorax closure is marked by elaborately orchestrated ECD. Thus, ECD in the heminotal epithelia is linked to dynamic spatiotemporal gradients of both Ft and Ds, which in turn determine the levels of adhesive Ft–Ds heterodimers formed at their cell perimeters. In a vertex model, we further mathematically establish these links between tissue-level gradients of Ft and Ds and the levels of Ft–Ds heterodimers formed therefrom. These simulations revealed that ECD in the vertex epithelium is the fallout from the balance of forces of contractility/elasticity versus cell expansion, the latter due to Ft–Ds heterodimer formation. Finally, by using developmental genetic tests, we further validated this in silico model of ECD regulation of Ft–Ds heterodimer formation, or cell–cell adhesion, via Ft and Ds gradients. These findings reveal a novel mechanism of regulation of ECD during morphogenesis in an epithelium by spatiotemporal modulation of heterophilic cell–cell adhesion.

RESULTS

Contralateral heminotal epithelia display epithelial cell size dynamics during thorax closure

The search for candidate cell–cell adhesion–based regulators of ECD requires the choice of an ideal model organ. For this purpose, morphogenesis of the adult thorax during pupal development is particularly interesting. The thorax (notum) of the adult *Drosophila* is a bilaterally symmetrical organ that is formed by zippering of two identical halves of epithelial cell sheets—the heminota—which are derived from the wing imaginal discs. Zippering of contralateral heminotal epithelia—also termed thorax closure—during early pupal development is marked by striking morphogenetic events, characterized by rapid changes in tissue size and contours (Martín-Blanco *et al.*, 2000). Thus we chose to examine heminotal epithelial morphogenesis during thorax closure and asked whether these display ECD in the first place.

Each heminotum represents the proximal region of a larval wing imaginal disc (Figure 1A), which is further divided into a medial and a lateral domain; the former is marked by expression of a transcription factor, Pannier (Pnr; Figure 1B; Calleja *et al.*, 2000). Immediately after pupariation, each heminotal epithelium displays eversion, in which it pops out through the overlaying larval epidermis (Martín-Blanco *et al.*, 2000; Pastor-Pareja *et al.*, 2004). Following eversion, the morphogenetic processes culminating in thorax closure lasts for ~1.5 h (4:30–6:00 h after puparium formation, APF) where the contralateral heminotal epithelia display elaborately orchestrated—and also nearly identical—morphogenetic movements reaching toward the body midline, followed by fusion (see Supplemental Video 1; Figure 1, C and D). To test whether heminotal epithelia display ECD during thorax closure, we first segmented their cell outlines, which were marked by DE-cadherin-GFP (Oda and Tsukita, 2001; Figure 1E) and calculated their apical cell sizes or apical cell surface areas (Figure 1F). We noted a wide range of cell sizes at 4:30 and 5:00 h APF (Figure 1, F–H), and their spatial distributions appeared largely comparable between the two contralateral heminotal epithelia. Upon culmination of thorax closure (6:00 h APF), cell sizes turn uniformly large throughout the fully expanded heminotal epithelium (Figure 1, F and I). In contrast, the spatial distribution of cell aspect ratios (cell elongation) in the heminotal epithelia remained comparable throughout the course of thorax closure (Supplemental Figure S2, A–C). Thus, the most dynamic period in morphogenesis of heminotal epithelia during thorax closure, marked by rapid changes in tissue contours, coincides with their ECD.
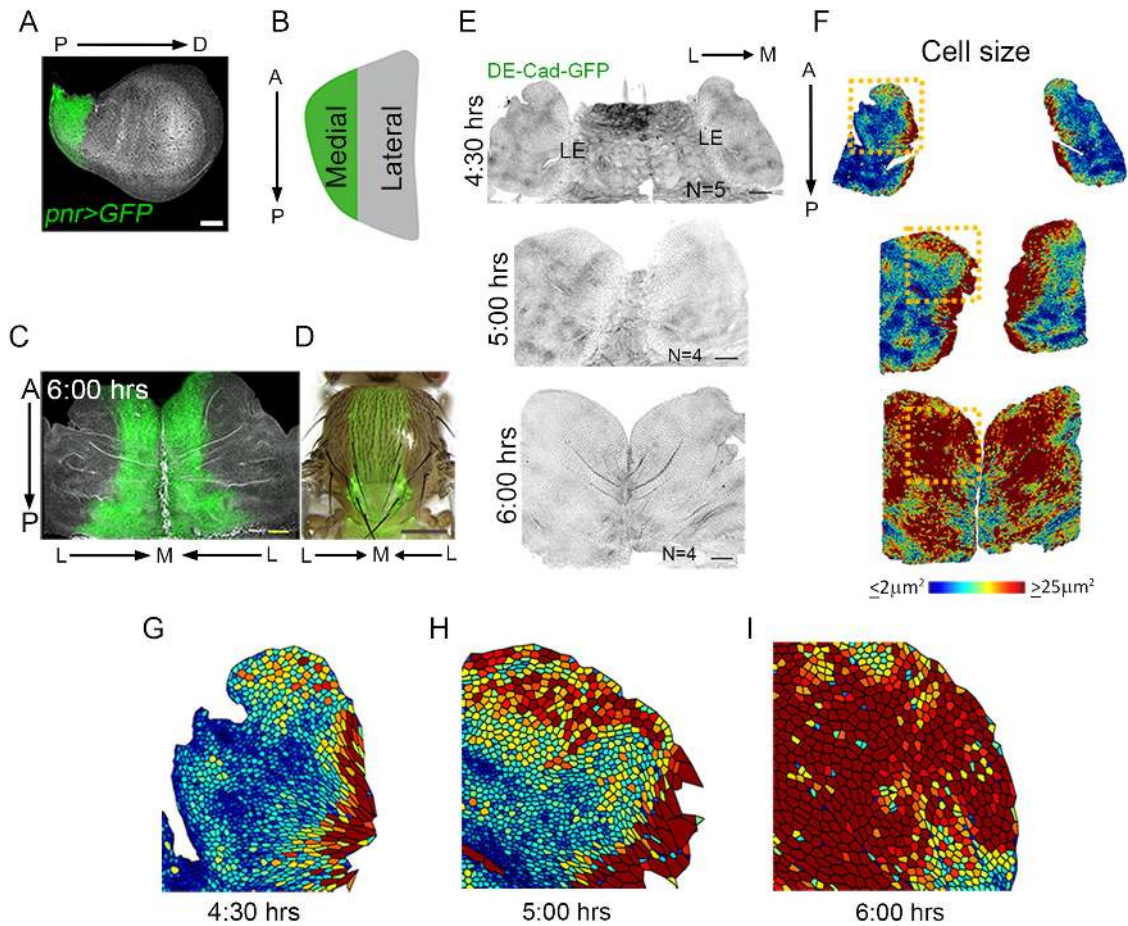
FIGURE 1: Heminotal epithelia of early pupa display ECD during thorax closure. (A) Domain of expression of *pnr-Gal4* driver (*pnr>GFP*) in late larval wing imaginal disc. (B) Cartoon representation of A in early pupal heminotum (4:30 h APF). (C) Medial domains (*pnr>GFP*, green) of a pair of contralateral pupal heminota at the end of thorax closure (6.00 h APF) and (D) in a freshly eclosed adult. (E) Contralateral heminotal epithelia during thorax closure where cell boundaries are marked by *ubi*-DE-Cad-GFP (gray) and their (F) segmented images quantified for cell size (apical cell surface area). (G–I) Boxed areas of F displayed at a higher magnification. Scale bars: 50 µm for A, C, and E; 200 µm for D. Abbreviation in this and subsequent images: L→M = lateral-to-medial axis, A→P = anterior-to-posterior axis. *N* = number of animals examined. APF = after puparium formation.

Expression gradients of Ft and Ds determine the levels of Ft–Ds heterodimers formed and the resultant ECD in heminotal epithelium

Given the previous reports on spatiotemporal regulation of Ds gradients in the wing imaginal disc epithelium (Clark *et al.*, 1995; Ma *et al.*, 2003), we examined the correlation between expression patterns of Ft and Ds—the two atypical cadherins displaying heterophilic cell–cell adhesion (Matakatsu and Blair, 2004, 2006)—and ECD in heminotal epithelia during thorax closure. We noted that Ft and Ds display contrasting and undulating gradients with mirrorlike symmetry in these contralateral heminota, in which the levels of Ft and Ds remain largely disparate along the anterior–posterior (A→P) axis at 5:00 h APF (Figure 2A). At the end of thorax closure (6:00 h APF), however, levels of expression of Ft and Ds plateaued, characterized by their elevated but shallow opposing gradients along the A→P axis (Supplemental Figure S4A).

We argued that, should Ft and Ds regulate heminotal ECD, their expression levels in any of the spatial domains of heminotal epithelium would dynamically correlate with cell sizes. To test this possibility, we first sought to quantify the levels of Ft and Ds at individual heminotal epithelial cell perimeters following their immunostaining.

A direct comparison between the immunofluorescence intensities of two proteins, however, is not possible, since their detections were made by two different primary antibodies and as many fluorochrome-tagged secondary antibodies. We overcame these limitations by normalizing the individual immunofluorescence intensities of Ft or Ds, respectively, to the fluorescence intensities of a single copy of Ft-eGFP (Brittle *et al.*, 2012) or Ds-eGFP (Brittle *et al.*, 2012) constructs in these heminotal epithelial cells (Supplemental Figure S3; for details, see *Materials and Methods*). These normalized quantities of Ft and Ds in individual cells of an entire heminotal epithelium were then plotted against their cell sizes. We note that during the active period of thorax closure (5:00 h APF), larger cells (red to yellow) displayed moderate to high levels of both Ft and Ds (Figure 2B; Box 1 in Figure 2B'), while in the smaller cells (light to dark blue cells) their levels were disparate: low Ft and high Ds or vice versa (Figure 2B; boxes 2 and 3 in Figure 2B'). At the end of thorax closure (6:00 h APF), heminotal epithelial cell sizes turn large (orange to maroon cells), coinciding with the largely uniform and elevated levels of Ft and Ds (Supplemental Figure S4B; Boxes 1–3 in Supplemental Figure S4B'). These observations therefore reveal an uncanny correlation between Ft and Ds levels in any given spatial
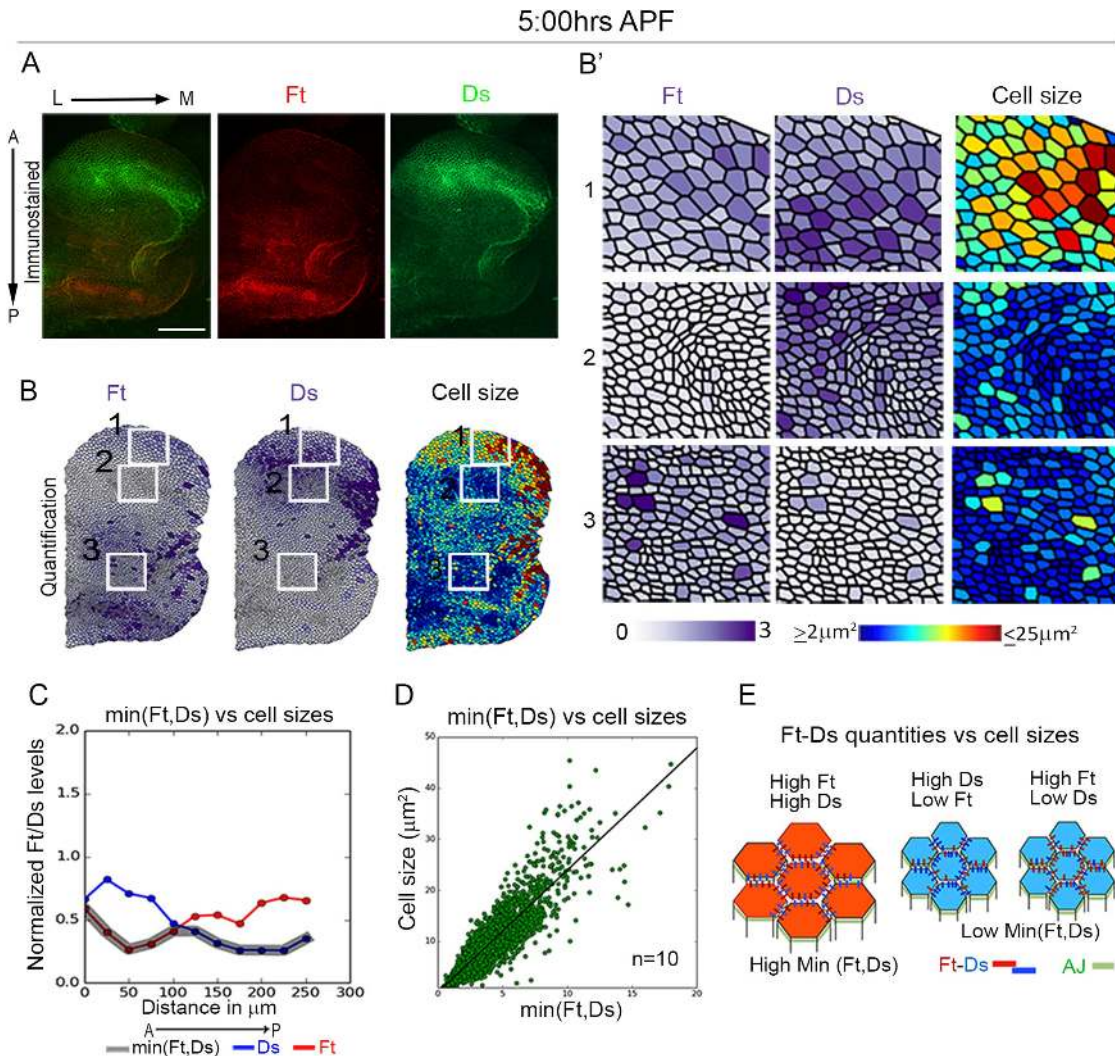
FIGURE 2: Gradients of Ft and Ds expressions in the pupal heminotal epithelia determine spatiotemporal levels of Ft–Ds heterodimer and cell sizes. (A) Immunolocalization and (B) quantification of Ft (red) and Ds (green) in heminotal epithelium; the image at the far right in B displays a quantification of their cell sizes. Individual quantifications of Ft and Ds at the cell perimeters were made after normalization of their immunofluorescence intensities, cell by cell, with those of a single copy of Ft-GFP and Ds-GFP, respectively (see Supplemental Figure S3 and *Materials and Methods*). These quantities of Ft and Ds are shown in a single color (purple, B) for ready visual comparison. Boxes 1, 2, and 3 from B are displayed at a higher magnification in B'. (C) Line plots showing the average levels of Ft (red), Ds (blue), and min(Ft,Ds) (thick light gray) along the A→P direction of this heminotal epithelium. Note that min(Ft,Ds) levels—a proxy for the levels of Ft–Ds heterodimer levels—invariably overlap with the lower of the two quantities Ft (red) or Ds (blue) in any given spatial domain. (D) Bivariate scatterplot of two quantities: cell size and min(Ft,Ds). (E) Cartoon displaying correspondence between the levels of Ft–Ds heterodimers and cell sizes (red to blue cells, red being the higher). Ft and Ds are indicated as colored bars. Although the cells here are shown as hexagons and with uniform elongation, results presented here suggest that the relationship between min(Ft,Ds) and cell size is not linked to cell shapes or cell elongation. Scale bar: 50 μm.

domain of the heminotal epithelium and their cell sizes: higher levels of Ft and Ds invariably displayed larger cell sizes than those where their levels were disparate.

Given that cell sizes are regulated by cell–cell adhesion, we further assumed that the levels of Ft and Ds in a given spatial domain of the heminotal epithelium dictate the level of adhesive Ft–Ds heterodimers formed at the cell perimeters and thereby the cell size. A test of this proposition requires quantification of the levels of Ft–Ds heterodimers in individual cells. Individual immunofluorescence intensities of Ft and Ds (see Figure 2B and Supplemental Figure S4B), however, cannot directly reveal the number of Ft–Ds

heterodimers formed at the cell perimeters. We circumvented this challenge of deriving the number of Ft–Ds heterodimer from those of Ft and Ds in a given cell perimeter in an indirect manner. We argued that in a heterophilic cell–cell adhesion system, numbers of heterodimers formed among cell neighbors will be rate-limited by the level of their binding partners (in this case Ft or Ds), whichever would be lower in a given spatial domain of heminotal epithelium, assuming all protein on the membrane can form heterodimers. This quantity—expressed mathematically as min(Ft, Ds)—then serves as a proxy for the quantities of Ft–Ds heterodimers formed and, by extension, the cell-expansive forces of cell–cell adhesion registered

at the cell perimeters. In agreement with this rationale, we noted that levels of min(Ft, Ds) estimated along the A→P axis of the heminota (thick gray line, Figure 2C; Supplemental Figure S4C) displayed an undulating pattern, overlapping with the levels of either Ft or Ds, whichever is lower in a given spatial domain (red or blue lines, Figure 2C; Supplemental Figure S4C). Further, bivariate plots revealed direct correspondence between cell sizes (Y axis) and the levels of min(Ft, Ds): that is, levels of Ft–Ds heterodimers throughout the heminotal epithelium (X axis, Figure 2D and Supplemental Figure S4D). In contrast, levels of min(Ft,Ds) did not display correspondence with cell aspect ratios (cell elongation) or the numbers of cell neighbors counted for individual cells: that is, their cell shape (Supplemental Figure S5, A and B).

Taken together—and notwithstanding the indirect estimation of Ft–Ds heterodimer—our results present a framework of Ft–Ds heterodimer-mediated regulation of heminotal cell sizes (Figure 2E). Here cell sizes are reduced when the levels of Ft and Ds are disparate, thereby lowering the levels of min(Ft,Ds) (blue cell, Figure 2E). In contrast, cell perimeters expand when levels of both Ft and Ds are comparable and high, which enhances their cell–cell adhesion as mirrored by their elevated levels of min(Ft,Ds) (red cells, Figure 2E).

Mathematical modeling of Ft and Ds gradient-linked epithelial cell size dynamics

Previous mathematical models of epithelial cell sheets suggest that regular hexagonal packing is a hallmark of low cell–cell adhesion and high cell contractility (Farhadifar et al., 2007). Such an epithelial cell sheet assumes minimal cell sizes, marked by their hexagonal shapes, and displays solidlike properties—as seen from the finite force required for their shear deformation. In contrast, when the strength of cell–cell adhesion is sufficiently high, epithelial cell sheets display an increase in their apical cell sizes due to cell-expansive forces exerted at their cell perimeters. Further, the overall mechanical properties of the tissue depends not only on the individual cells but also the intercellular adhesive interaction, and as a consequence, such an epithelium acquires the attributes of soft networks marked by their relatively easy deformation requiring minimal forces (Farhadifar et al., 2007; Bi et al., 2015; Alt et al., 2017). In the light of these mathematical models, ECD seen in heminotal epithelia during thorax closure could be interpreted as dynamic states of low and high cell–cell adhesion.

To formally test this emergent link between levels of cell–cell adhesion and cell size regulation, we mathematically recapitulated Ft and Ds gradients–linked cell size regulation using a vertex model (Farhadifar et al., 2007; Käfer et al., 2007; Alt et al., 2017). The vertex model is a physical representation of the configuration of cells in an idealized cell sheet based on a balance of opposing forces of cell contractility and cell–cell adhesion. In our vertex model, a balance of forces due to elasticity, actomyosin-driven cell contractility, and cell–cell adhesion was achieved by the minimization of an energy function (see Eq. 10 in Materials and Methods). Further, in the absence of a quantification of actomyosin-driven contractility and cell compressibility in the migrating heminotal epithelial cells, and for the sake of simplicity, these two parameters, cell contractility and elasticity, were kept constant in our vertex simulation. However, to factor the contributions of atypical cadherins, we also calculated forces of cell–cell adhesion generated by Ft–Ds heterodimers over and above those conferred by uniform levels of DE-cadherins. Further, spatiotemporal expression levels of Ft and Ds, as seen in vivo, were also taken into account by explicitly specifying them (for details, see Materials and Methods). Indeed, in agreement with our initial assumptions, our vertex model revealed spatiotemporal

dynamics of cell sizes and tissue expansion with changing gradients of Ft and Ds (Figure 3A and Supplemental Video 2), reminiscent of those seen in the heminotal epithelium in vivo (see Figure 2 and Supplemental Figure S4). For instance, at 4:30 h, domains marked by reduced cell sizes and tissue widths (blue arrows, Figure 3A) corresponded to those where the levels of Ft and Ds were disparate (Figure 3A), as seen in vivo (see Figure 2). Conversely, domains with moderate to high levels of both Ft and Ds displayed larger cell sizes, besides tissue expansion (red arrows, Figure 3A). Finally, our vertex model also recapitulated uniformly large cell sizes (Figure 3A) at the end of simulation (6:00 h), coinciding with the moderately elevated but shallow gradients of Ft and Ds in heminotal epithelium at the end of thorax closure (Supplemental Figure S4).

We further modeled the fallout of loss of Ft in a select group of cells in silico, such as could be induced in genetically mosaic heminotal epithelium in vivo. Simulation of mosaic vertex epithelium, created by removing Ft from different groups of cells, revealed reduction in cell sizes only in those spatial domains (middle and posterior, blue arrows, Figure 3B; Supplemental Video 3) where endogenous levels of Ft were higher than in the rest. Somatic loss of Ft in mosaic heminotal epithelium in vivo also revealed a reduction in cell sizes in ft mutant clones, but only in select spatial domains where its endogenous levels were relatively high (yellow stars; compare the magnified view of clones 1 and 2 in Figure 3C); this reduction in cell sizes in ft mutant clones is readily reconciled by the fact that loss of Ft–Ds heterodimer is anticipated to reduce the cell-expansive forces of cell–cell adhesion. Interestingly, at the clone margins (star in magnified box 2; Figure 3C; also see Dahmann and Basler, 2000; Jaiswal et al., 2006), Ds from the ft mutant cells displayed Ft–Ds heterodimers with their wild-type cell neighbors; hence reduction in cell sizes was not seen, further revealing a link between cell size enlargement and Ft–Ds heterodimer formation.

These observations in the mosaic epithelium, both in silico and in vivo, further reveal that Ft–Ds heterodimer–mediated cell–cell adhesion is one of the crucial regulators of cell size in the heminotal epithelium during thorax closure.

Loss of Ds or Ft gradients alter heminotal epithelial cell size dynamics and the tissue contour of the adult thorax

To further examine the fallout of cell–cell adhesion–mediated regulation of ECD on tissue morphogenesis, we examined the consequences of ubiquitous loss of Ds in our vertex model. Mathematically, consequences of loss of either Ds or Ft are indistinguishable in terms of their impacts on cell–cell adhesion, since both abrogate the formation of Ft–Ds heterodimers. We thus examined the consequences of knockdown of only one of the two atypical cadherins, say Ds, in half of the vertex epithelium, which was designated as its medial domain—à la its knockdown in the pnr-Gal4 domain in heminotal epithelium in vivo. This vertex epithelium displayed loss of Ft–Ds heterodimers (cells without pink edges in one half, Figure 4A), as anticipated, besides reduction in cell sizes (Figure 4A). Comparable outcomes were also noted upon knockdown of ds in the heminotal epithelium in vivo (pnr>ds-RNAi; Figure 4B) marked by reduction in their cell sizes (Figure 4B; magnified boxes 1 and 2 in Figure 4B'). Further, the overall cell size distribution plot in these heminota (red curves, Figure 4C) revealed a marked reduction in cell areas as compared with their control counterparts (green curves, Figure 4C). Likewise, ubiquitous loss of Ft in the medial heminota in vivo (pnr>ft-RNAi), too, revealed comparable reduction in their cell sizes (Supplemental Figure S6, A and B).

Regulation of ECD may also impact the final size and contour of the adult organ—in this case, the adult thorax. It may, however, be
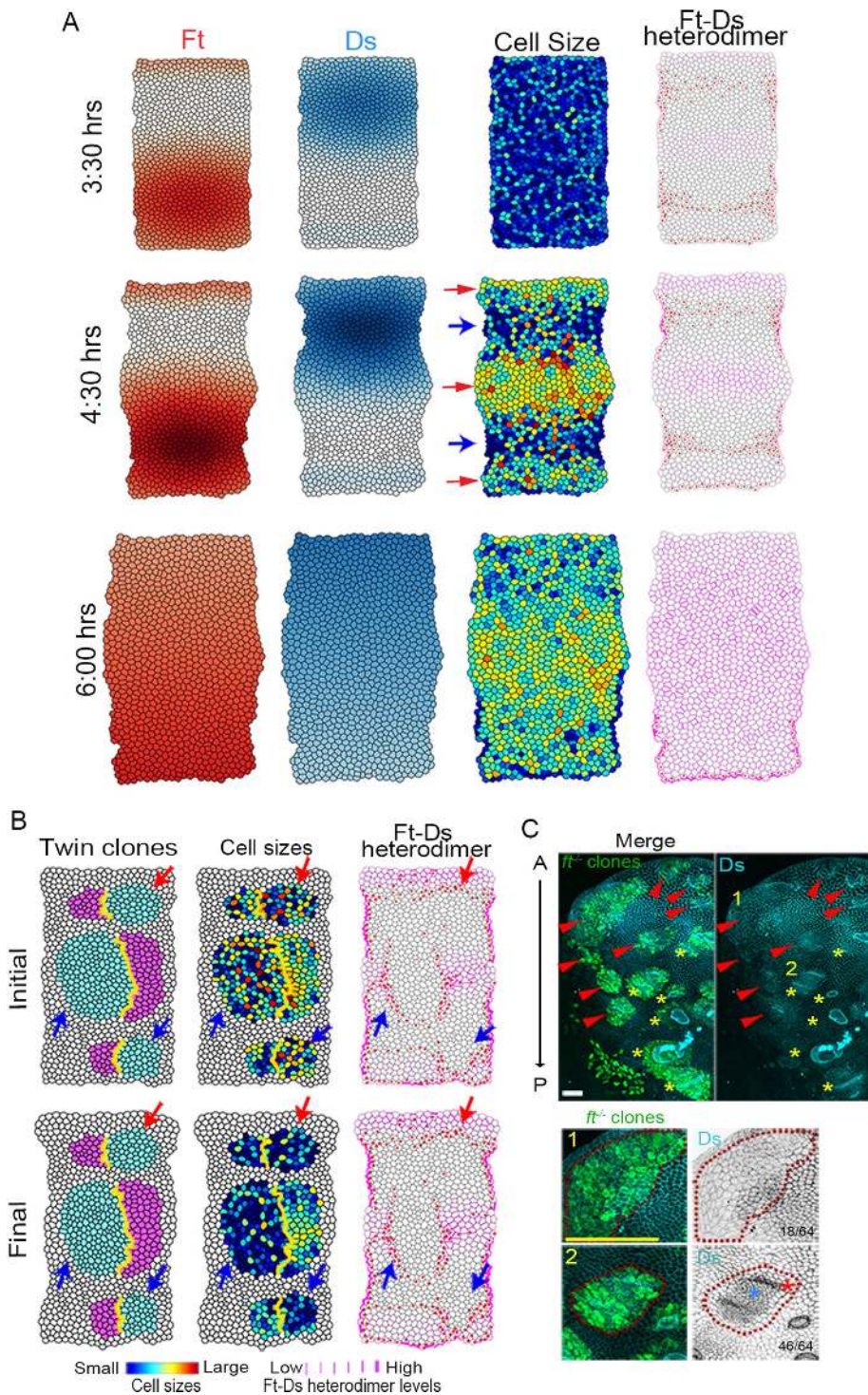
FIGURE 3: Mathematical modeling reveals correspondence between ECD and spatiotemporal gradients of Ft and Ds. (A) Snapshots of the vertex simulation of a heminotal epithelium (see Supplemental Video 2) in relation to the spatiotemporal gradients of Ft and Ds, and consequently cell sizes and the levels of Ft–Ds heterodimers (min(Ft,Ds)) at three designated time points during thorax closure. Note the correspondence between Ft and Ds spatiotemporal gradients, cell sizes, tissue expansion, and the level of Ft–Ds heterodimers. Cells marked by red dots are those that display asymmetric enrichment of Ft–Ds heterodimers at their edges above a certain threshold. Model parameters were set at $\overline{\Lambda}^{basal} = -0.1$, $\overline{\Gamma} = 0.1$, and $\eta = 2$. (B) Three ft mutant clones (cyan) and their respective wild-type twin clones (pink) in three different domains of an idealized vertex epithelium at an initial and final stage of simulation; the boundaries between the twin clones are marked by yellow lines. Note the reduction in cell sizes (light to dark blue) and in the levels of Ft–Ds heterodimers of the ft mutant clones located in the middle and posterior (blue arrows) domains, while in the one located anteriorly (red arrow), they appear

noted further that Ft and Ds atypical cadherins also regulate tissue growth; as a consequence, their individual losses results in tissue overproliferation (Bryant et al., 1988; Mahoney et al., 1991; Agrawal et al., 1995; Clark et al., 1995; Fanto et al., 2003; Cho et al., 2006; Jaiswal et al., 2006). Deciphering the ECD-linked phenotypic fallout of the loss of Ft and Ds could thus be confounded by their impact on tissue growth. To minimize this possibility, we thus examined the consequences of ft and ds knockdown only during a brief time window of thorax closure using the Gal4;Gal80[ts] system (McGuire et al., 2003; for further details, see *Materials and Methods*) with the rationale that this is likely to induce nominal cell proliferation and hence tissue overgrowth (Zeitlinger and Bohmann, 1999; Jaiswal et al., 2006). Indeed, knockdown of ds or ft, during this short time window of thorax closure, resulted in a change in overall contour of the adult thorax (see Figure 4D and Supplemental Figure S6C), without much change in their overall sizes. This characteristic adult thorax phenotype therefore reveals that perturbations in ECD during a phenocritical period of development—in this instance, thorax closure—affects the final adult organ shape.

Regulation of epithelial cell size dynamics by Ft–Ds heterodimers is delinked from their roles in planar cell polarity

It may be noted that linking Ft or Ds perturbation-induced phenotypes to merely a loss of regulation of cell–cell adhesion is further

comparable to its wild-type twin with respect to these parameters. Model parameters for wild-type as well as ft mutant clone simulations were $\overline{\Lambda}^{basal} = -0.1$, $\overline{\Gamma} = 0.1$, and $\eta = 2$. The wild-type expression levels of Ft and Ds ranged from 0.05 to 1. In ft mutant clones, the level of Ft was set to zero, corresponding to ft null clones. (C) A mosaic pupal heminotum displaying ft mutant clones (GFP, green) and immunostained for Ds (cyan). ft mutant clones marked by red arrowheads and yellow stars display cell sizes that are comparable to and smaller than their wild-type neighbors, respectively. Representative examples of these two categories of clones in domains marked as 1 and 2 are shown at a higher magnification in the panels on the right. Red star in magnified box 2 displays ft mutant cells near the clone boundary that display membrane localization of Ds, besides displaying normal cell sizes—that is, comparable to their wild-type neighbors, unlike those in the center of the clone (blue star). Scale bar: 50 μm.
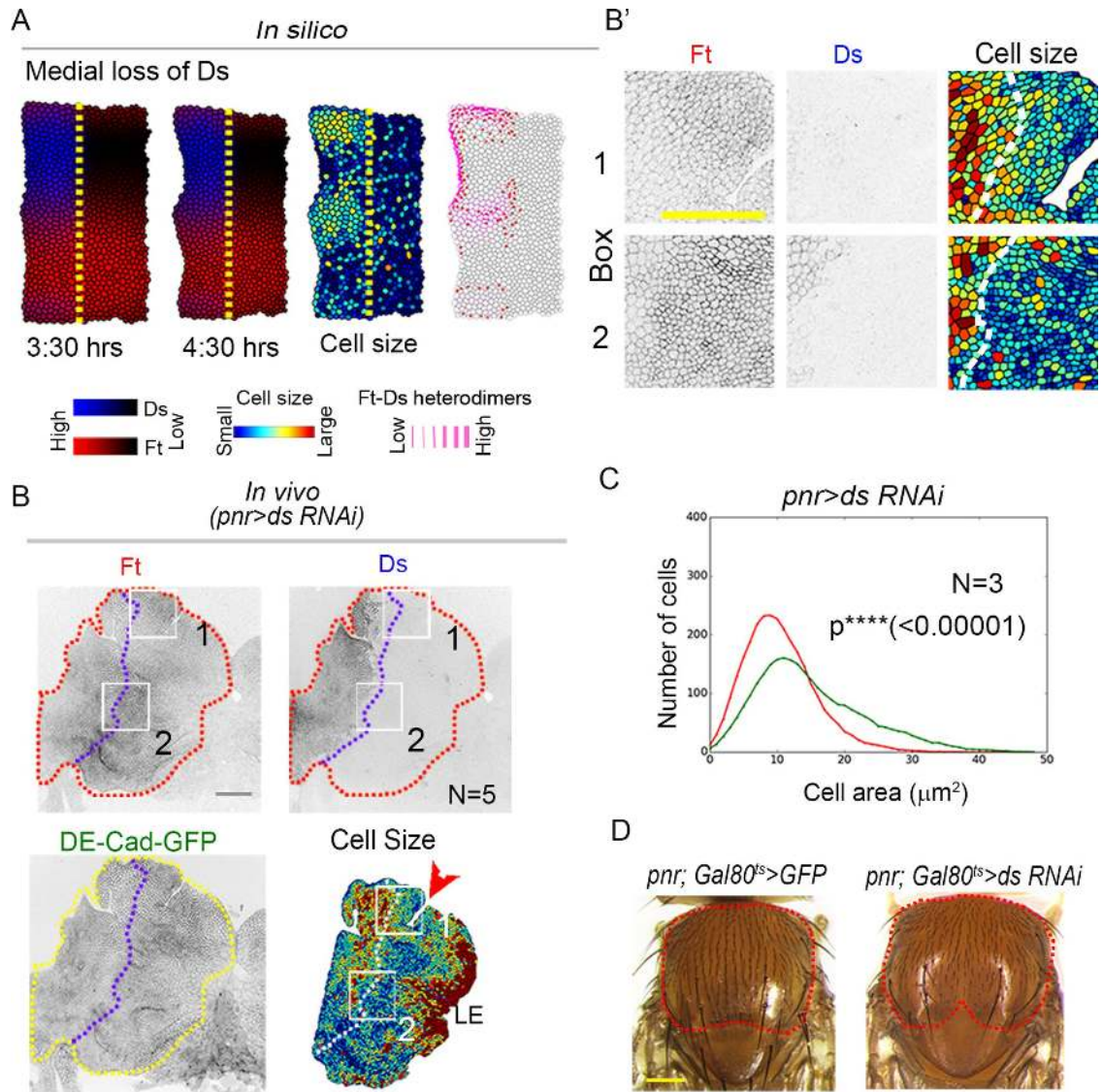
FIGURE 4: Knockdown of Ds gradients in heminotal epithelium also compromises its ECD. (A) A vertex model simulation where expression of Ds in the medial heminotal epithelium (right half of the yellow dashed line) was factored at a very low level at 3.30 and 4.30 h APF. Subsequent images display cell sizes and levels of Ft–Ds heterodimer; in the latter, cells marked by pink dots represent those that display asymmetric enrichment of Ft–Ds heterodimers at opposing cell edges. The model parameters were $\overline{\Lambda}^{basal} = -0.1$, $\overline{\Gamma} = 0.1$, and $\eta = 2$. (B) Heminotum at 5:00 h APF where Ds was knocked down (*pnr>ds-RNAi*) in the medial domain and immunostained for Ft (gray) and Ds (gray), while cell outlines were marked by DE-Cad-GFP (gray). Red arrowhead in the bottom right panel points at the anterior–medial domain, which displays loss of its characteristic large cells (compare with Figure 1, F and H). Boxes numbered 1 and 2 in B are displayed at a higher magnification in B'. (C) Distribution of cell sizes in control (green) and Ds-knockdown (red) heminotal epithelia. The Mann–Whitney test was used for comparison of the cell sizes using *R*. (D) Comparisons of the adult thorax phenotypes seen following Ds knockdown under the *pnr-Gal4* driver selectively during the period of thorax closure (see *Materials and Methods*). Note the overall change in the contour (red dotted line) of the adult thoraxes upon Ds knockdown during thorax closure as compared with that of the control (*tub-Gal80ts; pnr>GFP*). Scale bar: B, B' = 50 μm and D = 200 μm.

complicated by the fact that these atypical cadherins are also implicated in PCP-linked morphogenetic events that lasts for about 50 h, after thorax closure (Baena-López *et al.*, 2005; Bosveld *et al.*, 2012). Adult thorax derived from spatiotemporal knockdown of *ft* and *ds*, as shown above, does not induce any alteration in planar orientation of thoracic bristles—a PCP-linked phenotype (see Figure 4D and Supplemental Figure S6C), suggesting a role in ECD independent of PCP (Maung and Jenny, 2011).

To further confirm this, we looked into Four-jointed (Fj)—another component of Ft and Ds atypical cadherin-dependent global PCP regulators—a Golgi kinase that modifies Ft and Ds affinities by phosphorylating their extracellular cadherin repeats (Ishikawa *et al.*, 2008; Hale *et al.*, 2015). More recent studies have further implicated the Ft–Ds–Fj system in the regulation of migration of abdominal histoblasts (Arata *et al.*, 2017) and their planar orientation (Mangione and Martín-Blanco, 2018). We noted, however, that Fj
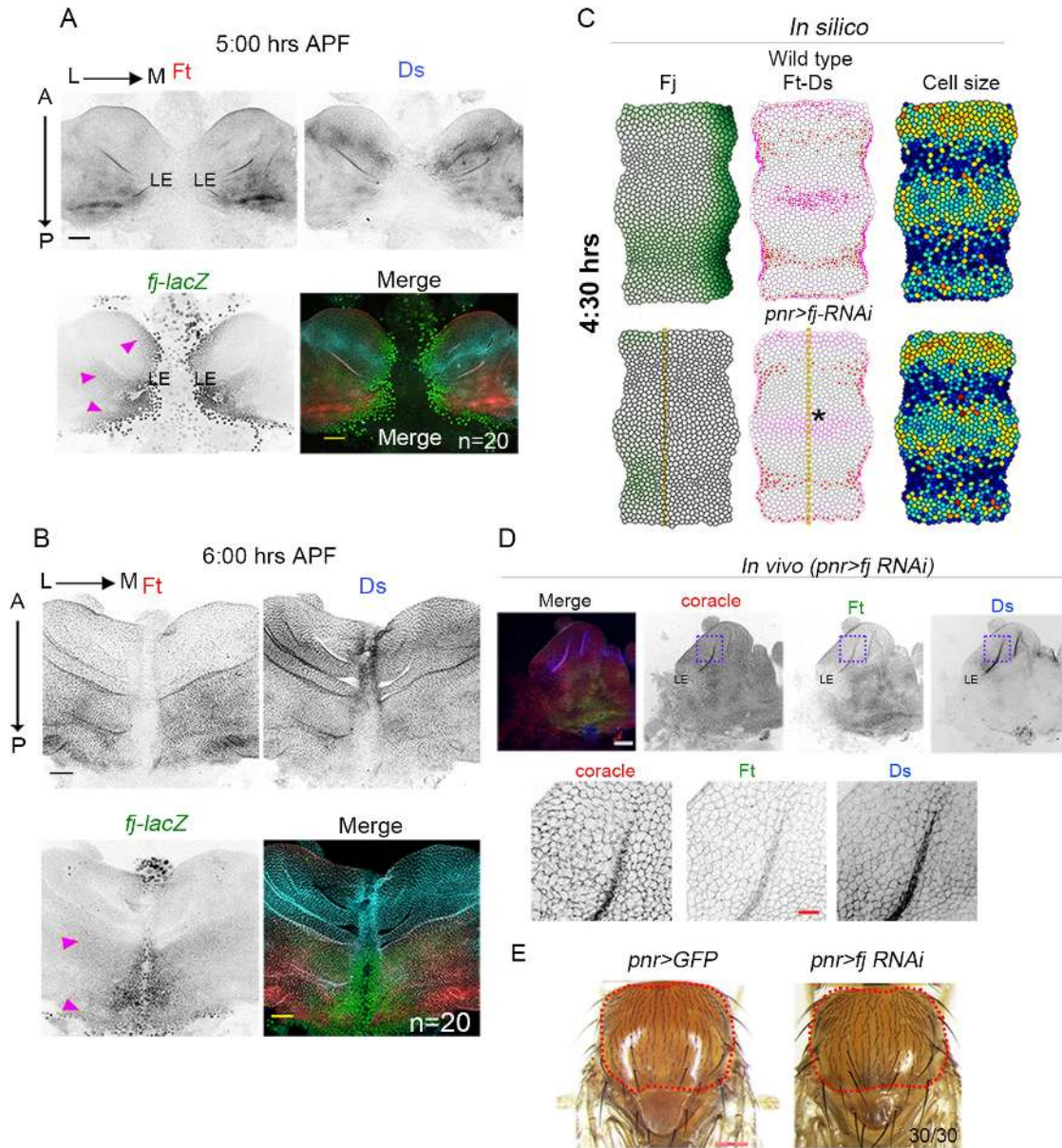
FIGURE 5: Knockdown of Fj kinase does not affect heminotal ECD. (A) Immunolocalization of Ft (red), Ds (cyan), and *fj-lacZ* (β-galactosidase, green) in pupal heminota (5.00 h APF). Note that the gradient of *fj-lacZ* along the medial-to-lateral (M→L) direction is elevated (pink arrowheads) at the leading edge (LE). (B) At the end of thorax closure (6:00 h APF), the Fj gradient displays a switch along the posterior-to-anterior (P→A) direction. (C) Vertex simulation of an idealized heminotum after factoring of the dynamic Fj expression (green) gradient, along with those of Ft and Ds (not displayed here, but see Figure 3). Note the reduction in the number of cells displaying asymmetric enrichment of Ft–Ds heterodimers (red dotted cells) when Fj is not factored (*pnr>fj-RNAi*), while overall distribution of the Ft–Ds heterodimers and cell sizes remains comparable to those where Fj gradient was factored (wild-type pattern in C). (D) Heminotal epithelium displaying knockdown of Fj (*pnr>fj-RNAi*) and immunostained for Coracle (red), Ft (green), and Ds (blue). Boxed areas in these images are shown at a higher magnification in the panel below. Note that expression of Ft and Ds seen here is comparable to that of wild-type counterparts (see Figure 2A), while their coracle-marked cell outlines suggest no change in cell sizes like those seen in the vertex simulation (C). (E) Adult thorax of control (*pnr>GFP*) and *pnr>fj-RNAi*. Red dotted lines mark the outlines of these thoraces, which reveal their comparable contours. Scale bar: A, B, D = 50 μm and 10 μm for magnified box of D, red scale bar; E = 200 μm.

gradients were restricted to only a limited area of the medial heminota, marked by its heightened expression at the leading edges (LE, Figure 5, A and B), whereas ECD was seen throughout the heminotal epithelium, sans the LE (Figure 1, F–I). Further, the vertex model also revealed that epithelial ECD was not affected when the Fj gradient was factored along with those of Ft and Ds (top panel in Figure 5C; also compare with 4:30 h in Figure 3A). Likewise, loss of Fj in medial heminota in silico did not affect their cell size (bottom panel, Figure 5C) despite reductions in the number of cells, which displayed asymmetrically enriched Ft–Ds heterodimers (star in bottom panel, Figure 5C). In vivo fallout of knockdown of *fj* in the medial domain also matched these features of vertex simulation:
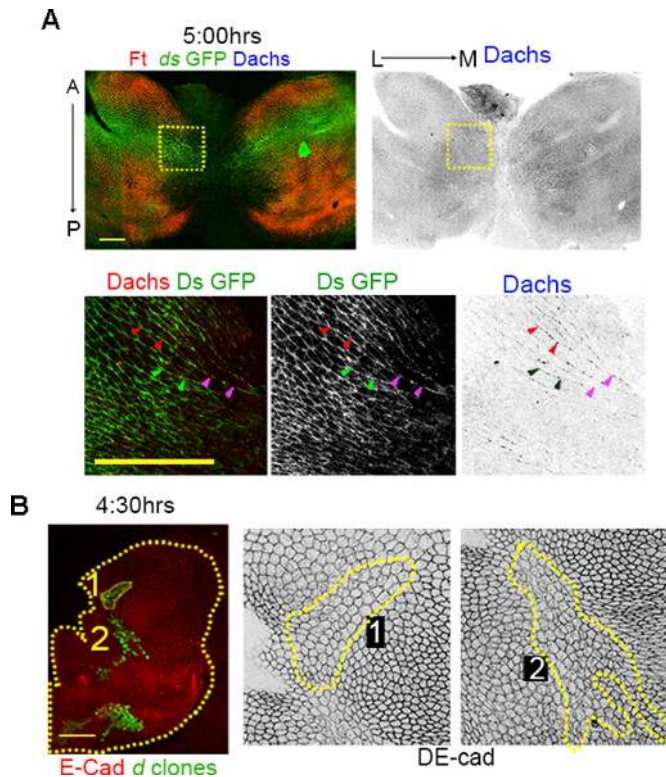
FIGURE 6: Recruitment of Dachs (D) at the Ft–Ds heterodimer-enriched cell edges does not influence heminotal ECD. (A) Pupal heminota expressing Ds-GFP (green) and immunostained for Ft (Red) and D (blue). Boxed area in A is displayed at higher magnification in the bottom panel: note the cell edges (colored arrowheads) marked by colocalizations of Ds-GFP and D. (B) A mosaic heminotum displaying d^{GC13} somatic clones (green) and immunostained for DE-Cad (red). Enlarged views of the clones marked 1 and 2 (yellow outlines) are displayed at higher magnification in the panels on the right (DE-Cad, gray). Cell sizes in these d mutant clones do not reveal any contrasting changes vis-à-vis their immediate cell neighbors. A total of 47 clones were scored from eight mosaic heminotal epithelia. Scale bar: 50 μm.

neither the overall expression pattern of Ft or Ds, nor heminotal cell sizes (Figure 5D) were affected. Not surprisingly, adult thorax formed post-larval-to-pupal knockdown of *fj* also failed to reveal a change in tissue contour (Figure 5E), unlike those seen following perturbations in the gradients of Ds (Figure 4D) or Ft (Figure 5C).

Apart from PCP, the Ft–Ds–Fj system also regulates tissue morphogenesis through one of its downstream effectors, an unconventional myosin, Dachs (D; Mao *et al.*, 2006). Asymmetric enrichment of Ds results in recruitment of its binding partner, D, at the cell edges, which then impacts oriented cell rearrangements during thorax morphogenesis (Bosveld *et al.*, 2012). Further, subcellular polarization of D also impacts the direction of cell elongation during mitosis, mitotic spindle alignment, and thereby the plane of orientation during cell division (Mao *et al.*, 2011), besides cell proliferation (Mao *et al.*, 2006). We noted recruitment of D along the edges of the heminotal epithelial cells, which also displayed Ft–Ds heterodimer enrichment during heminotal migration (Figure 6A). Knockdown of D strikingly compromised overall heminotal growth (Supplemental Figure S7), which was consistent with the requirement for D activity for epithelial cell proliferation (Mao *et al.*, 2006, 2011), which also hindered a clear assessment of its regulation of cell sizes, if any. To overcome these pleiotropic fallouts of ubiquitous loss of D, we examined the conse-

quences of loss of D in the somatic clones using the d allele, d^{GC13}. We noted that cell sizes in these clones (Figure 6B) were generally comparable to those of their wild-type neighbors.

These outcomes therefore suggest that modulation of selective affinities between Ft and Ds via Fj or recruitment of D on the edges of Ft–Ds-enriched cells largely do not impact regulation of ECD in heminotal epithelium.

DISCUSSION

Since its seminal proposition in the early 1960s (see Foty and Steinberg, 2005), the differential adhesion hypothesis (DAH) has helped explain morphogenetic processes, particularly those requiring separation of germ layers (gastrulation) and cell sorting (for detailed reviews, see Keller, 2002; Gumbiner, 2005; Halbleib and Nelson, 2006). These findings are consistent with the notion that homophilic cell–cell adhesion is likely to be stronger than heterophilic (Prakasam *et al.*, 2006). Unlike cell sorting induced by sharp changes in the levels of classical cadherin-based cell–cell adhesion, previous mathematical modeling proposed that nuanced modulation of cell–cell adhesion in an epithelium can induce dynamic changes in cell sizes and confer fluidlike attributes on an epithelium (Farhadifar *et al.*, 2007; Bi *et al.*, 2015; Alt *et al.*, 2017). These cell–cell adhesion proteins conferring nuanced and dynamic changes in cell sizes or ECD, however, have remained elusive. Here, for the first time, we reveal that heterophilic cell–cell adhesion mediated by the two atypical cadherins Ft and Ds represents one such, so far elusive, spatiotemporal regulators of nuanced ECD. In this novel paradigm of ECD regulation (Figure 7), the most crucial factors are the spatiotemporal gradients of Ft and Ds in the heminotal epithelia. Thus the level of Ft–Ds heterodimer formed—based on the lower of the two quantities, Ft or Ds, or min(Ft,Ds)—determine heminotal epithelial cell sizes: the higher the levels of Ft–Ds heterodimer, the greater the cell size and vice versa (Figure 2). Fallout of these adhesive interactions on heminotal cell sizes therefore essentially mirrors the emergent properties of spatiotemporal gradients of Ft and Ds. Our quantifications of adhesive Ft–Ds heterodimers at the cell perimeters, mathematical modeling of their regulation of cell sizes, and finally, validations of these predictions by developmental genetic tests collectively reveal a novel model of heterophilic adhesion–mediated regulation of ECD during epithelial morphogenesis (Figure 7).

Consistent with their regulation of cell–cell adhesion and thereby tissue fluidity (Farhadifar *et al.*, 2007; Bi *et al.*, 2015; Alt *et al.*, 2017), loss of Ft-Ds heterodimers impacts ECD-linked tissue morphogenesis such as the contour of the adult thorax (Figure 4D and Supplemental Figure S6C). In this regard, it is interesting to note that adult organ shapes and sizes can often display large variations in closely related species (Lawrence, 1992). It is thus tempting to speculate that diversity in organ size and shape could be attained by regulation of heterophilic cell–cell adhesion. Indeed, these speculations could be tested in terms of changes in the spatiotemporal regulation of Ft and Ds atypical cadherins among closely related *Drosophila* species that display diverse ranges of organ sizes and shapes.

We recognize that the idealized epithelium in the vertex model is a two-dimensional representation of a tissue that has a three-dimensional architecture. Further, tissue-level uniformity in cell elasticity and contractility in our vertex model are rather simplified assumptions made without accompanying experimental input. Examination of the cross-talk between the subcellular contractility with heterophilic cell–cell adhesion-dependent ECD, however, remains outside the scope of the present study. Notwithstanding
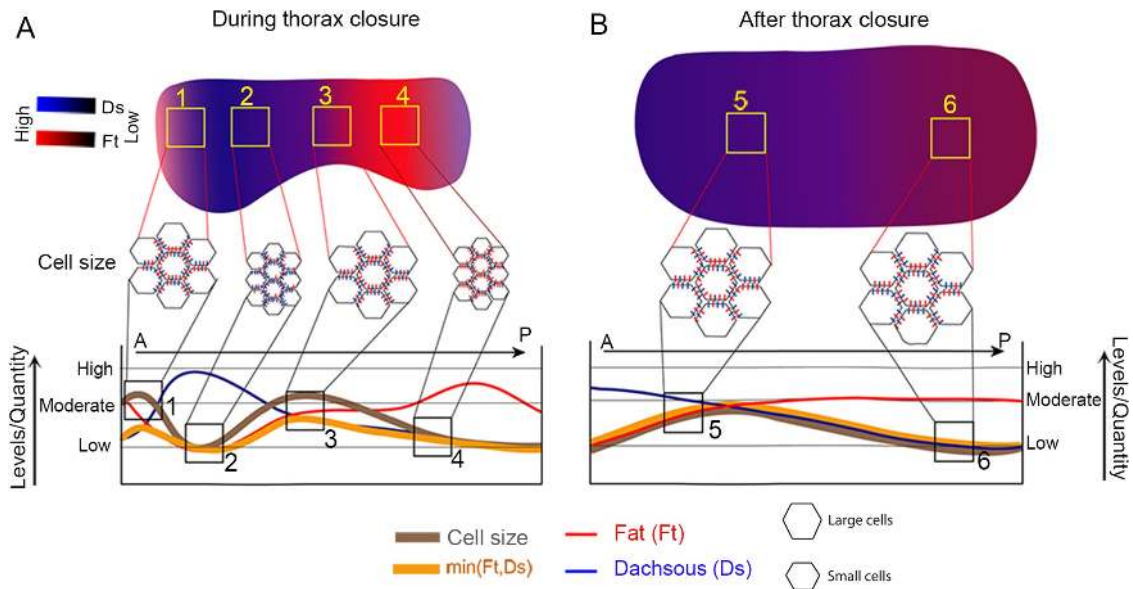
FIGURE 7: Spatiotemporal gradients of Ft and Ds underlie Ft–Ds heterodimer-mediated cell–cell adhesion and ECD. (A, B) Schematic representations of correspondence of Ft and Ds spatiotemporal gradients with the levels of Ft–Ds heterodimers [min(Ft,Ds)] and cell sizes during (A) and at the end of (B) thorax closure. Middle row displays an expanded view of heminotal cells in the zones marked 1–4 in A and 5 and 6 in B to reveal correspondence between the levels of Ft–Ds heterodimers formed and cell sizes. Bottom panels display plots for the levels of Ft (red line), Ds (blue line), and min(Ft,Ds) (thick orange line) in relation to their cell sizes (thick brown line). Note that during thorax closure, levels of min(Ft,Ds) varied along the A→P axis of the heminota with accompanying changes in cell sizes (A). In contrast, at the end of thorax closure Ft and Ds gradients plateau, as do the levels of min(Ft,Ds) and cell sizes across the entire epithelium (B).

these caveats, recapitulation of heminotal ECD commensurate with spatiotemporal gradients of Ft and Ds in our vertex model reveals an essential biophysical principle that connects Ft–Ds heterodimer-mediated cell–cell adhesion to cell size regulation. There could be additional tiers of complexities that link cell–cell adhesion with cell size regulation. For instance, while Ft–Ds heterodimers are formed at the subapical membrane, it is likely to impact the DE-cadherin-dependent cell–cell adhesion and cell contractility at the AJs. These are pointers toward as yet unexplored cross-talk between subapical Ft–Ds heterodimer–mediated cell–cell adhesion and other focal points in regulation of cell size and cell–cell adhesion (Gumbiner, 2005; Halbleib and Nelson, 2006; Lecuit and Lenne, 2007; Heisenberg and Bellaïche, 2013; Pinheiro and Bellaïche, 2018).

MATERIALS AND METHODS
Fly lines and husbandry
Drosophila genetic stocks used in this study were received either from the Bloomington Drosophila Stock Centre (BDSC) or the Vienna Drosophila Resource Centre (VDRC) or as gifts from other investigators. The following stocks were used: $ft^{fd}(ft^8)$ (Mahoney et al., 1991); d^{GC13} (Mao et al., 2006); $fj^{P1}(fj\text{-}lacZ)$ (Strutt et al., 2004); *UAS-nls.GFP* (BDSC #4776); *UAS-ds-RNAi* (VDRC#36219); *UAS-ft-RNAi* (VDRC #9396); *UAS-fj-RNAi* (VDRC #6774); *UAS-d-RNAi* (VDRC#12556); *pnr-Gal4* (Calleja et al., 2000); *tub-Gal80^{ts}* (BDSC #7017); *ubi-DE-cad-GFP* (Oda and Tsukita, 2001); *arm-GFP* (BDSC #60561); *ft-eGFP* (Brittle et al., 2012); *ds-eGFP* (Brittle et al., 2012); and *y,w,hs-flp* (BDSC #1929). All fly cultures, unless mentioned otherwise, were grown at 25°C on standard fly food media. Ectopic expressions of transgene were induced by *UAS/Gal4* (Brand and Perrimon, 1993) or *UAS/Gal4/Gal80^{ts}* (McGuire et al., 2003) for spatiotemporal regulation.

Staging, dissection, immunostaining, and imaging of pupal nota
APF pupal samples were selected at 0 h, as determined from the point when a third instar larva turns immobile and displays tanning of its cuticle at the ridge between the two anterior everted spiracles. These pupae were dissected in 1X phosphate-buffered saline (PBS) at chosen time points between 4:30 and 6:00 h APF, the time window for thorax closure (Martín-Blanco et al., 2000; Usui and Simpson, 2000), followed by fixing in 4% paraformaldehyde (PF) in PBS containing Triton X-100 (0.2%) for 1 h. This was followed by immunostaining, or the pupae were stained with phalloidin to mark actin using the standard protocol, and finally mounted under Vectashield (H-1000, Molecular Probes).

Primary antibodies used were Fat (1:250) (raised in rabbit, Santa Cruz Biotech, catalogue number: #sc-98850), Dachsous (1:250) (raised in goat, Santa Cruz Biotech, catalogue number: #sc26870), β-galactosidase (1:500) (raised in mouse, Sigma Aldrich, catalogue number: #A11132), DE-Cad (1:50) (raised in mouse, DSHB #DCAD2), Dachs (1:50) (raised in rat, gift from David Strutt, University of Sheffield), and Coracle (1:50) (gift from Richard Fehon, University of Chicago). Secondary antibodies used were tagged with Alexa 488, 555, or 633 (Molecular Probes). Confocal images were acquired using a Leica SP5 laser scanning confocal microscope. Images were processed using LAS AF software and Adobe Photoshop. Wherever relevant, fluorescent images were changed to grayscale to improve visualization.

Phenotypic study for adult thorax dimensions
The heminotal tissue contours, zippering defects, and adult thorax phenotypes were examined after knockdown of Ds, Ft, Fj, or D under the condition of simultaneous expression of *pnr-Gal4;tub-Gal80^{ts}* driver. In brief, egg laying was performed at 25°C and eggs

were cultured at 18°C until 214 h after egg laying (AEL) or 24 h before pupa formation. These larvae were further shifted to 29°C until 8 h APF and finally returned to 18°C until eclosion of adults. Images of adult flies thoraces were taken using a Leica M205 FA stereomicroscope at 10× magnification.

Generation of *ft* mutant clones

For mosaic studies, the flp/FRT system (Xu and Rubin, 1993) was used to generate loss-of-function clones of *ft^{fd}(ft^8)* (Jaiswal *et al.*, 2006) by heat shock to the larval cultures at 37°C (for 30 min) to induce flippase activity under the *hs-flp* transgene. One obvious caveat of mosaic studies of *ft* loss is their impact on cell proliferation (Jaiswal *et al.*, 2006) with respect to their neighbors, which may, in turn, affect their cell epithelial dynamics in an unknown manner. To avoid this potential pitfall, *ft* mutant somatic clones were generated at the mid-third instar stage (72–96 h AEL) to minimize the impact, if any, of their altered cell proliferation kinetics.

Quantitative image analysis

Image segmentation. To quantify various parameters, such as cell size, cell shape, or protein localization, at the level of individual cells, cell perimeters were identified using a custom-made image processing tool in MATLAB. Confocal images of the heminota with *ubi-DE-Cad-GFP*–marked cell boundaries were segmented using the watershed algorithm (Soille, 2004) to identify the individual cells. Prior to segmentation, noise in the images was reduced by image smoothing using two-dimensional median filtering (Lim, 1990) with a 3 × 3 matrix. To avoid false edge detection, the local minima were suppressed using the H-minima transformation (Soille, 2004). After segmentation, the vertices defining the boundary of each cell were identified by constructing a convex hull. In this method, therefore, each cell in the image was described as an ordered sequence of the coordinates of the points on the cell perimeter.

Apical cell size determination. An epithelium is a two-dimensional arrangement of three-dimensional cells; current imaging methods, however, do not permit precise measurement of the total volume of individual cells. Therefore, to obtain the cell volume, an approximation was made on the basis of the area of the apical cross-section of the cell. We estimated the apical cell size of each cell from the segmented image using the coordinates defining the boundary of that cell by using the shoelace formula for measuring the area of a polygon.

Measurement of cell aspect ratios. Quantification of the shape of any slender object is usually performed in terms of its aspect ratio, which is defined as the ratio of its shorter (width) to longer (length) sides. Therefore, aspect ratio can take any value ≥1. We used aspect ratio to define the degree of cell elongation, with a slight modification. We defined the cell elongation as follows:

$$\text{cell elongation} = 1 - \frac{\text{length of shorter side}}{\text{length of longer side}} = 1 - \frac{1}{\text{aspect ratio}} \quad (1)$$

We used this particular definition as the measure of cell elongation to make sure this quantity remained between 0 (for a perfectly circular cell) and 1 (for a highly elongated cell). For each cell, which is identified as a polygon by a sequence of points (r_i) using image segmentation, the center of the cell (r_c) is obtained by averaging as

$$r_c = \sum_{i=1}^{n} \frac{r_i}{n} \quad (2)$$

To calculate the length and width of a cell, its individual sides were divided into 10 equal segments and length and width were respectively defined as

$$r_{max} = \max_{1 \leq j \leq N} \left\{ \left| r_j - r_c \right| \right\} \quad (3)$$

$$r_{min} = \min_{1 \leq j \leq N} \left\{ \left| r_j - r_c \right| \right\} \quad (4)$$

where N is the total number of points on the cell periphery after its segmentation. Therefore the degree of cell elongation was calculated as

$$\text{cell elongation} = 1 - \frac{r_{min}}{r_{max}} \quad (5)$$

Normalization of Ft and Ds immunofluorescence to their respective endogenous protein quantities. We sought to quantify the levels of Ft and Ds proteins in the individual heminotal epithelial cells from their respective immunofluorescence, acquiring confocal images while keeping laser confocal scanning (Leica SP5) image acquisitions parameters such as laser power, laser intensity, gain, and noise reduction the same for each of their wavelength ranges. However, the fact that immunofluorescence of Ft and Ds were captured at two different wavelength ranges of excitation and emission (red wavelength range for Ft and far-red wavelength range for Ds) and that their 1° antibodies are likely to detect their respective epitopes with distinct efficiencies obviates the option of a direct comparison of the immunofluorescence of Ft and Ds to determine their relative quantities. We thus first normalized immunofluorescence intensities of Ft and Ds to their respective endogenous proteins as seen from the fluorescence intensity of GFP-tagged Ft (Ft-eGFP) or Ds (Ds-eGFP) as follows: we immunostained Ft-eGFP–marked heminotal epithelium for Ft in the red wavelength range at two time points of thorax closure (5:00 and 6:00 h APF). Intensities of Ft-eGFP (488–509 nm, green) fluorescence and Ft immunofluorescence (Alexa Fluor 555: 555–580, red) at each pixel in the heminotal epithelium were then plotted as scatterplots using the scipy library in Python (Supplemental Figure S2, A and B). The line of best fit for the individual scatterplot presented a slope and its average value from multiple heminota that provided a normalization factor, C_{Ft} Similarly, comparison of Ds-eGFP fluorescence (488–509 nm, green) with Ds immunofluorescence (far red: 633: 631–650 nm) provided a normalization factor, C_{Ds}. Quantitative estimates of Ft and Ds proteins in individual heminotal epithelial cells were then obtained as follows:

$$\text{quantitative level of Ft} = C_{Ft} \times I_{Ft} \quad (6)$$

$$\text{quantitative level of Ds} = C_{Ds} \times I_{Ds} \quad (7)$$

where I_{Ft} and I_{Ds} are the immunofluorescence of Ft (red channel) and Ds (far-red channel), respectively.

Quantification of Ft and Ds protein levels in individual cells and their cell boundaries. Samples of wild-type heminota, marked by arm-GFP, at 5:00 and 6:00 h APF were coimmunostained for Ft and Ds. Heminotal epithelial cell outlines were first ascertained by segmenting arm-GFP–marked cell boundaries. Absolute values of Ds and Ft from their respective immunofluorescence were then obtained by normalizing their respective normalization factors as mentioned above. Owing to their predominant localization, the quantification of Ft and Ds was restricted to the cell boundaries. So we took a striped region along the cell perimeter of three pixels

thickness. Summation of pixel intensity of a given fluorochrome thus provides a quantification of its total Ft or Ds for a given heminotal cell. For instance, cumulative fluorescence intensity for Ft, or total Ft level, in a given cell is calculated as

$$[Ft] = \sum\nolimits_{i \in C} Ft_i \qquad (8)$$

where Ft_i is the intensity of Ft in the ith pixel of the image and C is the set of image pixels belonging to a particular cell.

Estimation of Ft–Ds heterodimer levels for a cell based on min(Ft,Ds).

Ft–Ds heterodimers are formed at the interfaces of two cells. However, unlike the total levels of Ft or Ds in individual cells (Figure 2A), their quantification at the cell perimeters poses a challenge due to the limits of optical detection. So we estimated the Ft–Ds heterodimer levels using an indirect method, where we adopted a proxy quantification-based approach. This is based on the rationale that given their one-on-one binding to form Ft–Ds heterodimers, the level at the cell perimeters will be limited by one of the two quantities, Ft or Ds, whichever is lower in a given group of cells. This quantity, here referred as min(Ft,Ds)—a mathematical expression for the lower of the two quantities, Ft or Ds—then turns into a proxy measure for the levels of Ft–Ds heterodimers (thick gray lines in Figure 2C and Supplemental Figure S5C). Thus, with an assumption of high rates of heterodimer kinetics, the equilibrium levels of the Ft–Ds heterodimer formed by the ith cell are given by

$$H_i = \frac{[Ft]_i}{K_{Ft} + [Ft]_i} \frac{[Ds]_n}{K_{Ds} + [Ds]_n} + \frac{[Ds]_i}{K_{Ds} + [Ds]_i} \frac{[Ft]_n}{K_{Ft} + [Ft]_n} \qquad (9)$$

where $[Ft]_i$ and $[Ft]_n$ are the total Ft levels in the ith cell and its neighbors, respectively, and coefficients K_{Ft} and K_{Ds} depend on the details of the molecular interactions between Ft and Ds. This expression is based on the Hill equation widely used in the modeling of ligand–receptor binding kinetics (Attie and Raines, 1995). We have assumed that there is no cooperation or noncooperation in the Ft–Ds binding (Hill coefficient, $n = 1$). It can be seen that the two terms corresponding to Ft and Ds take different values depending on their respective availability, and now we face three possibilities:

1. $[Ft]_i > [Ds]_i$

   As the variation of Ft and Ds in the tissue is smooth (Figure 2), there are no sudden jumps in the expression levels of Ft and Ds; thus, the neighboring cells will also follow [Ft] > [Ds]. Therefore, the smaller number of Ds molecules saturate and thus the first term will attain a value of 1and the maximum possible heterodimer formation is proportional to $[Ds]_i$.

2. $[Ft]_i < [Ds]_i$

   In this case, the reverse will happen, where Ft molecules will saturate and the maximum possible heterodimer number is proportional to $[Ft]_i$.

3. $[Ft]_i = [Ds]_i$

   In this case, all Ft molecules will bind to Ds molecules and the heterodimer number will be equal to $[Ft]_i$, which is also equal to $[Ds]_i$.

   Therefore, it is evident that the maximum heterodimer formed by any cell is proportional to the level, whichever is lower between Ft and Ds in that cell. This level of Ft or Ds is designated by a mathematical expression, min(Ft,Ds), that refers to the lower quantity between Ft and Ds in a given cell. min(Ft,Ds), in turn, then represents a proxy for the levels of Ft–Ds heterodimers.

Statistical correlation between Ft–Ds heterodimer levels and cell sizes.

We next probed whether min(Ft,Ds) level or the levels of Ft–Ds-heterodimers, in brief, correlated with cell size and cell aspect ratios. Bivariate scatterplots were generated for cell sizes and aspect ratios (y-axis) against the min(Ft, Ds) (x-axis) for all the cells in individual segmented heminota of wild-type pupae. We also compared the change in cell sizes by plotting the cell size distribution curves for the wild type and testing samples where Ds or Ft were knockdown (pnr>ds-RNAi or pnr>ft-RNAi). Further, we used the nonparametric Mann–Whitney test for statistical comparison of the cell sizes between test and control.

Mathematical model

Vertex model of cell shape and size regulation in epithelia.

In the widely studied vertex model, the three-dimensional epithelial tissue is approximated as a two-dimensional system completely covered with nonoverlapping polygons, akin to a confluent cell monolayer. In this system, configuration of the cells is obtained by the minimization of the following energy function (Farhadifar et al., 2007):

$$E(R_i) = \sum_\alpha \frac{K_\alpha}{2}(A - A_\alpha)^2 + \sum_\alpha \frac{\Gamma_\alpha}{2} L_\alpha^2 + \sum_{i,j} \wedge_{ij} l_{ij} \qquad (10)$$

In this expression, K_α represents the modulus of area elasticity of the cells, $\wedge_{ij}$ is the adhesion strength at the edge shared between two adjacent cells, and Γ_α stands for cell contractility. Here cell adhesion strength, $\wedge_{ij}$, is an outcome of all of the cell–cell interactions, such as homophilic DE-cadherin interactions at the adherens junctions, whereas cell contractility Γ_α is driven by the actomyosin cytoskeleton. In general, the contractility parameter Γ_α depends on the localization of actomyosin on individual cell edges, and therefore each cell edge can have a different value. However, here we considered the actomyosin distribution to be uniform over the cell perimeter, and therefore we consider a single parameter describing the contractility of each cell edge. It has to be noted that, in general, the mechanical properties of the epithelium also depend on the viscoelastic nature of individual cells. However, in the context of thorax closure (with a large time scale), it is the viscous nature of the cells that prevails and the cell elasticity can be ignored. To study the effect of adhesive and contractile forces, we modeled the epithelium as a rectangular sheet of approximately 1000 cells. The adhesion parameter and contractility were nondimensionalized by $K_\alpha A_O^{3/2}$ and $K_\alpha A_O$, respectively (Farhadifar et al., 2007). Given the regular arrangement of the cells in the heminota (Figure 1), the values of these parameters for the simulation (taken from Farhadifar et al., 2007), corresponding to the solid phase of the epithelial tissue. The specific values taken for each case are specified in the respective figure legends (Figure 3A).

Effect of spatial gradients of Ft and Ds on tissue dynamics.

The heterophilic interactions between Ft and Ds from adjacent cells result in the Ft–Ds heterodimers at their apicolateral membranes (Ma et al., 2003). This gives rise to intercellular adhesive interactions, in addition to those registered due to the homophilic interactions of the DE-cadherins at the adherens junctions. Further, the level of Ft–Ds heterodimers formed among neighboring heminotal cells, and therefore their adhesive strengths, are considered to be dependent on the individual expression levels of Ft and Ds. Therefore, the total adhesion strength between the ith and jth cells can be written as

$$\wedge_{ij} = \wedge_{ij}^{basal} + \eta\left([Ft{-}Ds]_{i,j} + [Ds{-}Ft]_{i,j}\right) \qquad (11)$$

which is a combination of a basal level of adhesion ($\wedge_{ij}^{basal}$) and Ft–Ds heterodimer. Here, $[Ft–Ds]_{i,j}$ or $[Ds–Ft]_{i,j}$ represents the level of Ft–Ds heterodimer between the ith and jth cells, where Ft (or Ds) and Ds (or Ft) are contributed by the ith and jth cells, respectively. It has to be noted that for all the simulations we have assumed a fixed value for the basal level of cell–cell adhesion ($\wedge_{ij}^{basal} = -0.1$), although in vivo such a constant is a theoretical impossibility, given that even the level of DE-Cad at the AJs appears to display spatial variation, albeit small (see Supplemental Figure S1, A and B). An assumption of this nature, however, notwithstanding their spatial variability in heminotal epithelium, is essential to consider the fact that Ft–Ds heterodimers are not the sole mediators of cell–cell adhesion in the heminotal epithelium. Further, for our simulations, we have set $\eta = 2$, which leads to the relative strength of Ft–Ds heterodimer based cell–cell adhesion being weaker, stronger, or of a level similar to that of $\wedge_{ij}^{basal}$, depending on the level of Ft–Ds heterodimers formed at the cell edge.

Incorporation of expression gradients of Ft and Ds into the vertex model. We further considered Ft, Ds, and Fj expression patterns in the vertex model mimicking those seen in vivo during thorax closure (see Figure 3A). We first specified expression patterns for these proteins in the vertex model of heminotal epithelium at three time points: 3:30, 4:30, and 6:00 h APF, as seen during thorax closure in vivo (Figure 2A). Further, by linear interpolation, we obtained the continuous time-dependent expression patterns through these projected time intervals of thorax closure in our vertex model. Spatiotemporal dynamics of expression of Ft and Ds also resulted in spatiotemporal dynamics of adhesive strengths, namely, $\Gamma_{i,j}$, generated by Ft–Ds heterodimers formed between adjacent cells. Simulation of the vertex model of heminotal epithelium thus produces a time-dependent pattern of cell shape and size (see Supplemental Video 2).

Estimation of Ft–Ds heterodimer levels between two neighboring cells. To establish the relation between the gradients of Ft and Ds, we have followed the approach of Mani *et al.* (2013) (also see Jolly *et al.*, 2014). For a given Ft and Ds gradients, a cell can form heterodimers with its neighboring cells in two ways, by contributing Ft or Ds to the shared edge with its neighbor, whereas the neighboring cell contributes Ds or Ft, respectively. These two contributions, Ft or Ds, by a cell lead to the formation of opposing polarities of heterodimers Ft–Ds and Ds–Ft at its edge. It is assumed that heterodimers of a given polarity promote the formation of their own type and oppose the formation of the opposing polarity. Therefore, the equation for the heterodimer formation can be written as

$$\frac{d[Ft–Ds]_{i,j}}{dt} = k_f \left(1 + k_p [Ft–Ds]_{i,j}\right)\left([Ft]_i - \sum_{j \in N_i} [Ft–Ds]_{i,j}\right)$$

$$\times \left([Ds]_j - \sum_{k \in N_j} [Ds–Ft]_{j,k}\right)$$

$$- k_b [Ft–Ds]_{i,j} \left(1 + k_o [Ds–Ft]_{i,j}\right) \qquad (12)$$

where

1. $[Ft–Ds]_{i,j}$: level of Ft–Ds heterodimer between cell i and j
2. $[Ds–Ft]_{i,j}$: level of Ds–Ft heterodimer between cell i and j
3. $[Ft]_i$: level of Ft in cell i
4. $[Ds]_i$: level of Ds in cell i

5. N_α: neighbors of cell i
6. k_f, k_p, k_b, k_o: rate constants.

Effect of Fj on Ft–Ds heterodimer formation. As reported earlier, the phosphorylation of Ft and Ds by kinase Fj impacts their mutual affinities toward each other (Ishikawa *et al.*, 2008; Hale *et al.*, 2015). This results in a very high affinity between phosphorylated Ft ($[Ft^p]$) and unphosphorylated Ds ($[Ds^u]$) as opposed to a very low affinity between unphosphorylated Ft ($[Ft^u]$) and phosphorylated Ds ($[Ds^p]$). Therefore, Fj levels in the cells, too, influence intercell interactions, besides the levels and gradients of Ft and Ds (Hale *et al.*, 2015). With these roles of Fj, the rate of Ft–Ds formation can be modified to

$$\frac{d[Ft–Ds]_{i,j}}{dt} = k_f \left(1 + k_p [Ft–Ds]_{i,j}\right)\left([Ft]_i \left(1 + k_{fj} [Fj]_i\right) - \sum_{j \in N_i} [Ft–Ds]_{i,j}\right)$$

$$\times \left([Ds]_j \left(1 - k_{fj} [Fj]_j\right) - \sum_{k \in N_j} [Ds–Ft]_{j,k}\right)$$

$$- k_b [Ft–Ds]_{i,j} \left(1 + k_o [Ds–Ft]_{i,j}\right) \qquad (13)$$

where $[Fj]_j$ is the level of Fj in the ith cell and k_{fj} is a constant depicting the rate of phosphorylation of Ft and Ds by Fj.

Simulation of genetic manipulations in the vertex model

To study the effects of the genetic manipulations mimicking those seen in vivo, for instance, their losses in the somatic clones of the *ft* mutant (Figure 3C) or knockdown of Ds or Fj in the medial domain of heminotal epithelium, the corresponding losses were considered in the vertex model. For the case of somatic loss of *ft* or medial knockdown of Ds, Fj was also factored. For simulation of loss of Ft in somatic clones, we selected a group of cells as lacking the Ft protein (equivalent to *ft* null mutant somatic clones), whereas an adjacent group of cells were marked as their wild-type twins. Further, following the characteristic of *ft* mutant and its twin described earlier (Jaiswal *et al.*, 2006), namely, overproliferation in the mutants, larger clone size (cell numbers) and altered cell–cell adhesion marked by its smooth clone boundary were observed. In contrast, the wild-type twins are smaller, with a not-too-smooth clonal boundary. In the initial configuration (3:30 h APF) in the $ft^{-/-}$ clones value of Ft, $[Ft]_i = 0$ was set while keeping the Ds and Fj levels unchanged, while in the wild-type twin clones the level of Ft was kept unchanged, namely $[Ft]_i$. During the plotting of the cell geometries of the heminota, the twin clones were colored differently for their ready visualization. Simulating ubiquitous loss of Ds or Fj in the medial domain mimicking in vivo perturbations, we considered their individual losses in the half of the simulated heminotal epithelium akin to the medial region in vivo and specified the levels of Ds as $[Ds]_i = 0$ and $[Fj]_i = 0$, respectively.

REFERENCES
Agrawal N, Joshi S, Kango M, Saha D, Mishra A, Sinha P (1995). Epithelial hyperplasia of imaginal discs induced by mutations in *Drosophila* tumor

suppressor genes: growth and pattern formation in genetic mosaics. Dev Biol 169, 387–398.

Alt S, Ganguly P, Salbreux G (2017). Vertex models: from cell mechanics to tissue morphogenesis. Philos Trans R Soc B Biol Sci 372.

Arata M, Sugimura K, Uemura T (2017). Difference in Dachsous levels between migrating cells coordinates the direction of collective cell migration. Dev Cell 42, 479–497.e10.

Attie AD, Raines RT (1995). Analysis of receptor–ligand interactions. J Chem Educ 72, 119.

Baena-López LA, Baonza A, García-Bellido A (2005). The orientation of cell divisions determines the shape of Drosophila organs. Curr Biol 15, 1640–1644.

Bi D, Lopez JH, Schwarz JM, Manning ML (2015). A density-independent rigidity transition in biological tissues. Nat Phys 11, 1074–1079.

Bosveld F, Bonnet I, Guirao B, Tlili S, Wang Z, Petitalot A, Marchand R, Bardet PL, Marcq P, Graner F, Bellaïche Y (2012). Mechanical control of morphogenesis by Fat/Dachsous/Four-jointed planar cell polarity pathway. Science 336, 724–727.

Brand AH, Perrimon N (1993). Targeted gene expression as a means of altering cell fates and generating dominant phenotypes. Development 118, 401–415.

Brittle A, Thomas C, Strutt D (2012). Planar polarity specification through asymmetric subcellular localization of Fat and Dachsous. Curr Biol 22, 907–914.

Bryant PJ, Huettner B, Held LI, Ryerse J, Szidonya J (1988). Mutations at the fat locus interfere with cell proliferation control and epithelial morpho-genesis in Drosophila. Dev Biol 129, 541–554.

Butler MT, Wallingford JB (2017). Planar cell polarity in development and disease. Nat Rev Mol Cell Biol 18, 375–388.

Calleja M, Herranz H, Estella C, Casal J, Lawrence P, Simpson P, Morata G (2000). Generation of medial and lateral dorsal body domains by the pannier gene of Drosophila. Development 127, 3971–3980.

Cho E, Feng Y, Rauskolb C, Maitra S, Fehon R, Irvine KD (2006). Delineation of a Fat tumor suppressor pathway. Nat Genet 38, 1142–1150.

Clark HF, Brentrup D, Schneitz K, Bieber A, Goodman C, Noll M (1995). Dachsous encodes a member of the cadherin superfamily that controls imaginal disc morphogenesis in Drosophila. Genes Dev 9, 1530–1542.

Dahmann C, Basler K (2000). Opposing transcriptional outputs of Hedge-hog signaling and engrailed control compartmental cell sorting at the Drosophila A/P boundary. Cell 100, 411–422.

Devenport D (2014). The cell biology of planar cell polarity. J Cell Biol 207, 171–179.

Durney CH, Harris TJC, Feng JJ (2018). Dynamics of PAR proteins explain the oscillation and ratcheting mechanisms in dorsal closure. Biophys J 115, 2230–2241.

Fanto M, Clayton L, Meredith J, Hardiman K, Charroux B, Kerridge S, McNeill H (2003). The tumor-suppressor and cell adhesion molecule Fat controls planar polarity via physical interactions with Atrophin, a transcriptional co-repressor. Development 130, 763–774.

Farhadifar R, Röper J-C, Aigouy B, Eaton S, Jülicher F (2007). The influence of cell mechanics, cell–cell interactions, and proliferation on epithelial packing. Curr Biol 17, 2095–2104.

Foty RA, Steinberg MS (2005). The differential adhesion hypothesis: a direct evaluation. Dev Biol 278, 255–263.

Godt D, Tepass U (1998). Drosophila oocyte localization is mediated by differential cadherin-based adhesion. Nature 395, 387–391.

Goodrich LV, Strutt D (2011). Principles of planar polarity in animal development. Development 138, 1877–1892.

Gumbiner BM (2005). Regulation of cadherin-mediated adhesion in morphogenesis. Nat Rev Mol Cell Biol 6, 622–634.

Halbleib JM, Nelson WJ (2006). Cadherins in development: cell adhesion, sorting, and tissue morphogenesis. Genes Dev 20, 3199–3214.

Hale R, Brittle AL, Fisher KH, Monk NAM, Strutt D (2015). Cellular interpretation of the long-range gradient of Four-jointed activity in the Drosophila wing. ELife 4, e05789.

Hayashi T, Carthew RW (2004). Surface mechanics mediate pattern formation in the developing retina. Nature 431, 647–652.

Heisenberg C-P, Bellaïche Y (2013). Forces in tissue morphogenesis and patterning. Cell 153, 948–962.

Ishikawa HO, Takeuchi H, Haltiwanger RS, Irvine KD (2008). Four-jointed is a Golgi kinase that phosphorylates a subset of cadherin domains. Science 321, 401–404.

Jaiswal M, Agrawal N, Sinha P (2006). Fat and Wingless signaling oppositely regulate epithelial cell-cell adhesion and distal wing development in Drosophila. Development 133, 925–935.

Jolly MK, Rizvi MS, Kumar A, Sinha P (2014). Mathematical modeling of sub-cellular asymmetry of Fat-Dachsous heterodimer for generation of planar cell polarity. PLoS One 9, e97641.

Käfer J, Hayashi T, Marée AFM, Carthew RW, Graner F (2007). Cell adhesion and cortex contractility determine cell patterning in the Drosophila retina. Proc Natl Acad Sci USA 104, 18549–18554.

Keller R (2002). Shaping the vertebrate body plan by polarized embryonic cell movements. Science 298, 1950–1954.

Lawrence PA (1992). The Making of a Fly: The Genetics of Animal Design, Oxford, UK: Blackwell Scientific Publications.

Lecuit T (2005). Adhesion remodeling underlying tissue morphogenesis. Trends Cell Biol 15, 34–42.

Lecuit T, Lenne P-F (2007). Cell surface mechanics and the control of cell shape, tissue patterns and morphogenesis. Nat Rev Mol Cell Biol 8, 633–644.

Lim JS (1990). Two-Dimensional Signal and Image Processing, Upper Saddle River, NJ: Prentice-Hall.

Loza O, Heemskerk I, Gordon-Bar N, Amir-Zilberstein L, Jung Y, Sprinzak D (2017). A synthetic planar cell polarity system reveals localized feedback on Fat4–Ds1 complexes. eLife, https://elifesciences.org/articles/24820.

Ma D, Yang C, McNeill H, Simon MA, Axelrod JD (2003). Fidelity in planar cell polarity signalling. Nature 421, 543–547.

Mahoney PA, Weber U, Onofrechuk P, Biessmann H, Bryant PJ, Goodman CS (1991). The fat tumor suppressor gene in Drosophila encodes a novel member of the cadherin gene superfamily. Cell 67, 853–868.

Mangione F, Martín-Blanco E (2018). The Dachsous/Fat/Four-Jointed pathway directs the uniform axial orientation of epithelial cells in the Drosophila abdomen. Cell Rep 25, 2836–2850.e4.

Mani M, Goyal S, Irvine KD, Shraiman BI (2013). Collective polarization model for gradient sensing via Dachsous–Fat intercellular signaling. Proc Natl Acad Sci USA 110, 20420–20425.

Mao Y, Rauskolb C, Cho E, Hu W-L, Hayter H, Minihan G, Katz FN, Irvine KD (2006). Dachs: an unconventional myosin that functions downstream of Fat to regulate growth, affinity and gene expression in Drosophila. Development 133, 2539–2551.

Mao Y, Tournier AL, Bates PA, Gale JE, Tapon N, Thompson BJ (2011). Planar polarization of the atypical myosin Dachs orients cell divisions in Drosophila. Genes Dev 25, 131–136.

Martin AC, Kaschube M, Wieschaus EF (2009). Pulsed contractions of an actin-myosin network drive apical constriction. Nature 457, 495–499.

Martín-Blanco E, Pastor-Pareja JC, García-Bellido A (2000). JNK and decapentaplegic signaling control adhesiveness and cytoskeleton dynamics during thorax closure in Drosophila. Proc Natl Acad Sci USA 97, 7888–7893.

Matakatsu H, Blair SS (2004). Interactions between Fat and Dachsous and the regulation of planar cell polarity in the Drosophila wing. Develop-ment 131, 3785–3794.

Matakatsu H, Blair SS (2006). Separating the adhesive and signaling functions of the Fat and Dachsous protocadherins. Development 133, 2315–2324.

Matis M, Axelrod JD (2013). Regulation of PCP by the Fat signaling pathway. Genes Dev 27, 2207–2220.

Maung SMTW, Jenny A (2011). Planar cell polarity in Drosophila. Organogenesis 7, 165–179.

McGuire SE, Le PT, Osborn AJ, Matsumoto K, Davis RL (2003). Spatiotempo-ral rescue of memory dysfunction in Drosophila. Science 302, 1765–1768.

Oda H, Tsukita S (2001). Real-time imaging of cell–cell adherens junctions reveals that Drosophila mesoderm invagination begins with two phases of apical constriction of cells. J Cell Sci 114, 493–501.

Pastor-Pareja JC, Grawe F, Martín-Blanco E, García-Bellido A (2004). Invasive cell behavior during Drosophila imaginal disc eversion is mediated by the JNK signaling cascade. Dev Cell 7, 387–399.

Pinheiro D, Bellaïche Y (2018). Mechanical force-driven adherens junction remodeling and epithelial dynamics. Dev Cell 47, 3–19.

Prakasam AK, Maruthamuthu V, Leckband DE (2006). Similarities between heterophilic and homophilic cadherin adhesion. Proc Natl Acad Sci USA 103, 15434–15439.

Soille P (2004). Morphological Image Analysis: Principles and Applications, Berlin: Springer-Verlag.

Somorjai IML, Martinez-Arias A (2008). Wingless signalling alters the levels, subcellular distribution and dynamics of Armadillo and E-cadherin in third instar larval wing imaginal discs. PLoS One 3, e2893.

Strutt H, Mundy J, Hofstra K, Strutt D (2004). Cleavage and secretion is not required for Four-jointed function in Drosophila patterning. Development 131, 881–890.

Usui K, Simpson P (2000). Cellular basis of the dynamic behavior of the imaginal thoracic discs during *Drosophila* metamorphosis. Dev Biol 225, 13–25.

Widmann TJ, Dahmann C (2009). Wingless signaling and the control of cell shape in *Drosophila* wing imaginal discs. Dev Biol 334, 161–173.

Wodarz A, Stewart DB, Nelson WJ, Nusse R (2006). Wingless signaling modulates cadherin-mediated cell adhesion in *Drosophila* imaginal disc cells. J Cell Sci 119, 2425–2434.

Xu T, Rubin GM (1993). Analysis of genetic mosaics in developing and adult *Drosophila* tissues. Development 117, 1223–1237.

Zeitlinger J, Bohmann D (1999). Thorax closure in *Drosophila*: involvement of Fos and the JNK pathway. Development 126, 3947–3956.

Zmurchok C, Bhaskar D, Edelstein-Keshet L (2018). Coupling mechanical tension and GTPase signaling to generate cell and tissue dynamics. Phys Biol 15, 046004.